Switching of Hybrid Improper Ferroelectricity in Oxide Double Perovskites

Gayathri Palanichamy,[†] M. J. Swamynathan,[†] Monirul Shaikh,[†] Ayana Ghosh,[*,‡] and Saurabh Ghosh[*,†]

[†]*Department of Physics and Nanotechnology, Faculty of Engineering and Technology, SRM Institute of Science and Technology, Kattankulathur - 603 203, Tamil Nadu, India*

[‡]*Computational Sciences and Engineering Division, Oak Ridge National Laboratory, Oak Ridge, TN 37831, USA*

E-mail: ghosha@ornl.gov; saurabhghosh2802@gmail.com

Abstract

In ABO_3-type perovskite oxides with *Pnma* symmetry, rotation (Q_{R+}, $a^0a^0c^+$) and tilt (Q_T, $a^-a^-c^0$) of BO_6 octahedra are the two primary order parameters. These order parameters establish an inherent trilinear coupling with anti-ferroelectric A-site displacement (Q_{AFE}) to form the low symmetry phase. The symmetry is further lowered in double perovskite oxides due to A/A′ cation ordering. It in turn makes these systems polar via hybrid improper ferroelectric (HIF) mechanism, primarily driven by Q_{R+} and Q_T . Naturally, it has been believed that functionalities such as polarization can also be switched by tuning these primary order parameters. However, mystery around finding switching mechanism still remains. Our study based on density functional theory calculations combined with finite temperature molecular dynamics simulations shows that the polarization switching is a two-step process, driven by out-of-phase rotation (Q_{R-}, $a^0a^0c^-$ when $Q_T = 0$ or, $a^-a^-b^-$ when $Q_T \neq 0$). A series of polar double

perovskite oxides such as $KLnFeOsO_6$ (Ln = Sm, Gd, Dy, Tm (lanthanides) and Y (rare earth), all belonging to $P2_1$ symmetry, are considered in this investigation. The polarization switching ($\vec{P}$) occurs at a very high temperature of $\sim$ 1150 K through a phase transition, from a polar ($P2_1$) phase with $\vec{P}+$ to $\vec{P}$- via a non-polar $P4/n$ phase. The switching itself is metastable in nature. However, the switching (both polarization and spin state) is only observed for a very short period of time ($\sim$ 23 ps) that poses limitation on using such mechanism in memory device realization. We demonstrate a concurrent heating-cooling procedure to overcome such shortcoming. Simulations conducted at 600 K further imply that long lasting switching can be achieved, at least for 1.2 ns for 600 K, and ideally infinity, if the material is heated just above the T_C followed by rapid cooling to a temperature below T_C.

Introduction

One of the primary challenges in the field of multiferroics[1–3] is to identify stable candidates that exhibit strong coupling between electric polarization ($\vec{P}$) and magnetization ($\vec{M}$) with potential device applications.[4,5] Polarization in such materials are either driven by the zone-centered lattice instability[6,7] making the origin of ferroelectricity proper or catered to structural distortions leading to improper[8] or hybrid-improper ferroelectrics (HIFs).[9–13] Among the family of perovskites exhibiting such coupling, magnetic HIFs are interesting.[9,13] Here, symmetry breaking occurs due to structural instability, resulting in strong magnetoelectric coupling between $\vec{M}$ and $\vec{P}$.[13] Considering layered perovskite in the form of superlattice or Ruddlesden-Popper phase, the microscopic origin of $\vec{P}$ is due to non cancellation of layered polarization in two successive layers, whereas, the origin of $\vec{M}$ occurs due to spin canting. Thus, in these systems both $\vec{P}$ and $\vec{M}$ are too small, limiting their applications as desired.

Double perovskite oxides (DPOs) with chemical formula $AA'BB'O_6$ are promising in this context. In DPOs, the AA′-sites are occupied by an alkaline-earth or rare-earth ion. Transition metal ions are located at the BB′ sites. Individual structural or functional modes

and coupling[14–16] between them generally drive electronic, polar and magnetic functionalities in DPOs. The common modes of interest are in-phase (Q_{R+}, $a^0a^0c^+$), out-of phase (Q_{R-}, $a^0a^0c^-$) rotations, tilt (Q_T, $a^-a^-c^0$), A-site anti-ferroelectric displacement (Q_{AFEA}). In DPOs, the (BB′) sublattices typically order in rock-salt while (AA′) sublattice can order in layered [L], rock-salt [R] or columnar [C] form. Once distortion pattern of ($a^-a^-c^+$) is imposed, layered AA′ and rock-salt ordered BB′ phase (A[L]B[R]) transforms to non-centrosymmetric polar structure with $P2_1$ symmetry. The low symmetry phase $P2_1$ is es-

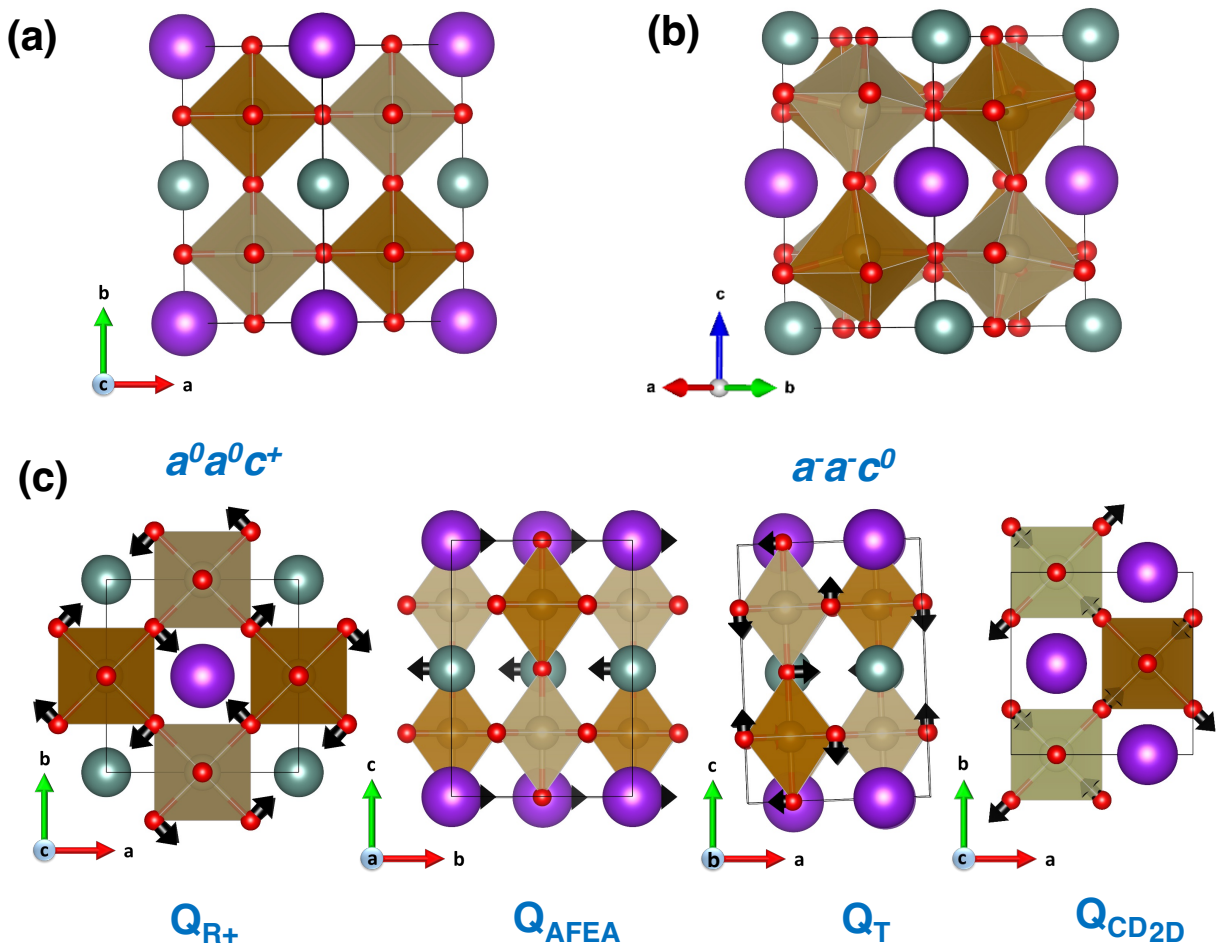

Figure 1: Representative structural models of (a) high symmetry $P4/nmm$, (b) low symmetry $P2_1$ phases, (c) key functional modes such as rotation (Q_{R+}), anti-ferroelectric A-site displacement (Q_{AFEA}), tilt (Q_T) and charge disproportion mode ($Q_{CD_{2D}}$) of polar double perovskite oxides.

tablished via trilinear coupling between rotation Q_{R+} , Q_T, and Q_{AFEA}. This phase is polar

and exhibits magnetic ordering originating from the BB′ site. There are two different magnetic cations located at ordered B and B′ sites leading to ferrimagnetic (FiM) ground state with large net magnetization. The origin behind sizeable microscopic layered polarization in these systems is hybrid improper in nature. Therefore, finding DPOs with stable cation ordering at AA′ site opens up avenues to design novel multiferroics.

Recent study lead by Ghosh et al.[17] sheds light on accessing such structures by redefining the condition of achieving stable A-site layered ordering to be the trilinear coupling between Q_{R+}, Q_T, and Q_{AFEA}. Density functional theory (DFT) calculations performed on a series of DPOs as computationally designed by combining various A-site cations with elements from Group IA, Group IIA, lanthanides, rare earth with B-site cations selected from blocks of $3d$, $4d$ and $5d$ transition metal elements are considered in the work. It shows that the layered A-site cation ordered phase with B-site as rock-salt (with antiferromagnetic (G-type AFM) ordering) can be stabilized for compounds with $3d$-$5d$ combinations with high confidence. For other DPOs within the same series, A-site cations tend to disorder, making it more difficult to form stable cation ordering. Magnetic ordering at B-site does not have much effect on cation ordering at A-site. A simple expression utilizing information on structures such as tolerance factor, oxidation states and radii of cations is derived to obtain difference in energy between other types of ordering with respect to that of clear layered ordering. Causal learning in combination with traditional machine learning (ML) further elucidates systematic controls of the primary order parameters such as Q_{R+} and Q_T over other functional modes (such as Q_{R-}, Q_{AFEA}) along with geometric changes driving both phase transitions and cation ordering. Altogether, it becomes evident that if trilinear coupling is established in ground state for DPOs, presence of second-order Jahn-Teller distortion no longer serves as the primary criteria for stabilizing A-site layered ordering. In addition, it lifts yet another constraint from the design rules of DPOs, stating that compounds without d^0 state at B-sites can still exhibit multiferroic behavior. The DPOs such as $KYFeOsO_6$, $KSmFeOsO_6$, $KGdFeOsO_6$, $KDyFeOsO_6$ and $KTmFeOsO_6$ as listed in this study are expected to be good

polar magnetic double perovskite candidates. However, the switching mechanism behind these functionalities are not yet well-understood.

This is where our present study becomes relevant which focuses on investigating the fundamental mechanisms behind the nature of functionalities along with their tunable origins. Past research efforts[9–11,13,18] suggest that the primary order parameters such as Q_{R+} and Q_T along with Q_{AFEA}, $Q_{CD_{2D}}$ drive many key properties in DPOs such as linear magnetoelectricity, ferromagnetism, polarization and metal-to-insulator transition. Such observations also have lead to proposition of identifying these primary order parameters as well as other structural distortions as the control variables behind switchable functionalities.[18–23] However, a robust cognizance of the switching mechanism detailing the conditions of polarization reversal and how it occurs, is still missing.

In this work, we have utilized a combination of DFT and *ab initio* molecular dynamics (AIMD) simulations, performed on a series of DPOs, namely $KLnFeOsO_6$ (Ln = Sm, Gd, Dy, Y and Tm) with B-site rock-salt and A-site layered ordering with $P2_1$ crystal symmetry. Our DFT computations show that these DPOs have sizeable polarization (12-19 $\mu C/cm^2$), switching barrier (20-50 meV/formula unit) and magnetization (total magnetic moment combining spin and orbital contributions $\sim$ 4.2-4.3 μ_B), respectively. The magnetism here is non-collinear in nature of type $A_xG_yG_z$ where m_x is of A-type (A_x) AFM, m_y and m_z are of G-type AFM (G_yG_z) ordering. Finite temperature simulations are performed systematically between 100 K and 2100 K. At room temperature (T = 300 K), the polar $P2_1$ phase is the stable phase. We define the switching temperature T_S as the temperature at which $\vec{P}+$ switches to $\vec{P}-$ for the first time. The range of T_S varies between 1150 K to 1200 K for the DPOs considered in this study. The polarization vector switches from [010] to $[0\bar{1}0]$ via switching path driven by out-of-phase rotation (Q_{R-}, $a^0a^0c^-$ when Q_T=0 or, $a^-a^-b^-$ when $Q_T \neq 0$). The spin state is also reversed between S=1 and S=3/2 around the same T_S. Here, we define the spin state for the entire material system based on the G-type magnetic ordering and electronic states of d orbitals of the B ($3d^5$) and B′ ($5d^3$) cations.

Our study shows that Q_{R-} is not one of the primary order parameters driving the polarization and spin state switching. It is contrary to the mechanisms proposed in the literature.[20–22] There is a linear relationship between T_S and tolerance factor τ. Overall, this study finds the fundamental mechanism behind how switching occurs in a series of DPOs which is expected to be useful in designing memory devices.

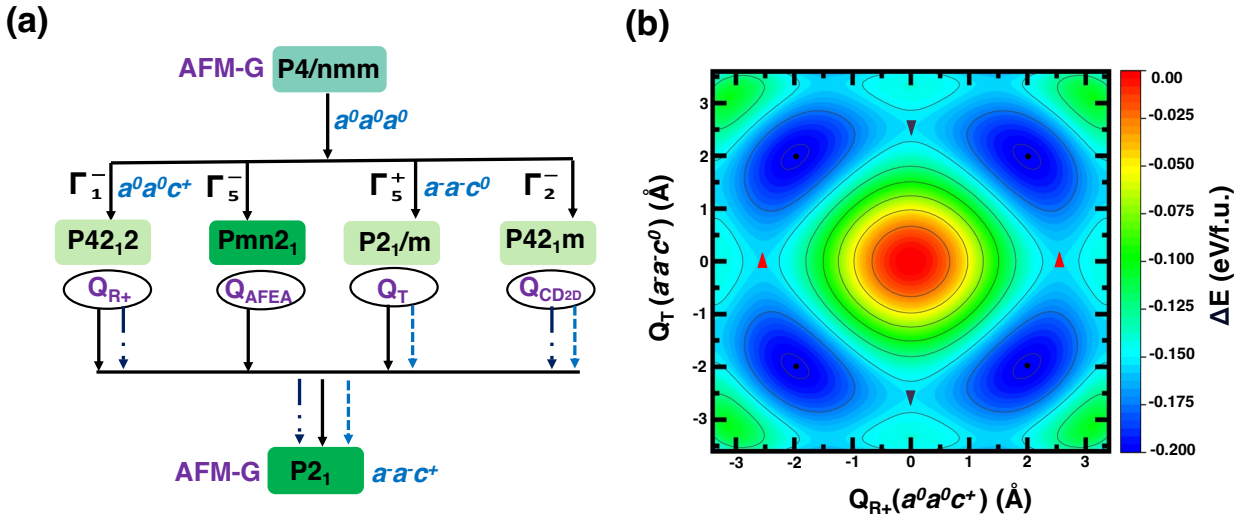

Figure 2: (a) Illustration of group-subgroup relations between high-symmetry $P4/nmm$ ($a^0a^0c^0$) and low-symmetry $P2_1$ ($a^-a^-c^+$). The intermediate phases belong to crystal symmetry group of $P4212$, $Pmn21$, and $P21/m$ and $P421m$. (b) Energy surface contour of $KYFeOsO_6$ with respect to the primary order parameter Q_{R+} ($a^0a^0c^+$) and Q_T ($a^-a^-c^0$). The black dots represent possible minimum structures while the black triangles (downward) indicate $P4212$ structures where tilt is absent. The red triangles (upward) indicate $P21/m$ structure where rotation is absent.

Computational Details

DFT computations:

First-principles calculations are performed using DFT[24] with projector augmented wave (PAW) potentials and within generalized gradient approximation,[25] as implemented in Vienna *ab initio* simulation package (VASP).[26,27] The exchange-correlation part is approximated by PBEsol functional.[28] We have used a $\sqrt{2}a \times \sqrt{2}a \times 2c$ pseudo cubic cell containing

total 20 atoms for all computations. The converged cell dimensions and volume are listed in the Table S1 of Supporting Information. Brillouin zone integration is performed with a Γ centered 6 $\times$ 6 $\times$ 4 K-point mesh following the crystal symmetry. A cutoff energy of 520 eV is set for all computations. Spin-orbit coupling[29] is introduced for all calculations. An effective ($U_E = U$ - J_H) Hubbard parameter is assumed to account for on-site Coulomb interaction for $3d$ states of Fe ($U_E = 4.5$ eV) and $5d$ states of Os ($U_E = 1.0$ eV), respectively. The specific U_E values are chosen to ensure correct account of oxidation states along with convergence of local magnetic moments (spin and orbital) at BB$'$ sites. Additional details on (i) noncollinear spin and orbital magnetic moments of all DPOs, (ii) the vector representation of $A_xG_yG_z$ magnetic configuration, and (iii) relative energy difference between various noncolinear magnetic configurations are listed in Table S2, Figure S1, Table S3 and Table S4 of Supporting Information, respectively. We have considered a non-collinear magnetism of type $A_xG_yG_z$ for the cations located at BB$'$-sites which is the lowest energy magnetic configuration. Spontaneous polarization is computed using the Berry phase approach.[30] All geometry relaxations are carried out until changes in the total energy between relaxations steps are within 1×10^{-6} eV and atomic forces on each of the atoms were smaller than 0.01 eV/. For each calculation assuming non-collinear magnetic configurations, the total energy is converged to 1×10^{-8} eV. For all DPOs, we consider the $P4/nmm$ ($a^0a^0a^0$) phase as high symmetry (Figure 1 (a)) and $P2_1$ ($a^-a^-c^+$) phase as low symmetry (Figure 1 (b)).

Finite temperature simulations:

The primary aim of this study is to investigate how switching occurs in polar DPOs at various temperatures utilizing AIMD simulations. At the initial stages, it is important to determine the initial structure for the simulation as well as the temperature range which is suitable to capture the polarization switching dynamics. Hence, we have first performed two different series of AIMD simulations on one of the DPOs, namely $KYFeOsO_6$. We assumed two initial structures, one as the ground state polar $P2_1$ phase and another as the high

symmetry P4/nmm phase, followed by running the simulations at constant temperature range between 100 K and 2100 K fort 120 ps. From these set of simulations, it became evident that the polarization switching only occurs at a very high temperature, beyond 1100 K. Moreover, irrespective of which structure we assume as the initial one, the system always goes to an equilibrated polar $P2_1$ phase below T_c and to non-polar $P4/n$ phase above T_c. A discussion on approximation of T_c from these simulations is included in the Results and Discussion section. Based on these set of simulations, we have selected the temperature range between 1200 K and 2100 K with initial structure of each simulations as the polar $P2_1$ phase. We note that polarization switching is a metastable state which corresponds to the phase transition from a polar phase ($\vec{P}$+) to ($\vec{P}$-) via non-polar phase. Therefore, we are essentially capturing the behavior of the system in this transition region and the factors driving such transition.

Our methodology complies with that adapted for studying oxide materials at higher temperature.[31–33] It is also consistent with the computational approach utilized in literature to understand the effect of temperature and electric field on polarization switching for two-dimensional (2D) ferroelectric van der Waals crystals.[34,35] The canonical NVT[36] ensemble with Nose-Hoover thermostat approach is adapted to keep a temperature constant during AIMD simulations.[37,38] The Brillouin zone is sampled at the gamma point. Initial velocities are set randomly according to Maxwell–Boltzmann distribution.[39] Each system is then allowed to relax for 50 ps with a time step of 1 fs. We have tracked the displacements of A and A$'$ cations from the centrosymmetric position for the entirety of all simulations. The AMPLIMODES (symmetry mode analysis) and PSEUDO (a program for pseudo-symmetry search) packages are used to analyze the structural modes as involved during the switching process.[40,41] We have repeated our calculations with 2×2×2 K-mesh (total 8 irreducible K-points) for $KYFeOsO_6$ for T = 1150 K. The results obtained with Gamma-point and the 2×2×2 comply with each other as listed in Table S5 and presented in Figure S2 of the Supporting Information. A qualitative assessment on polarization switching derived from

gamma point calculations does not differ much from that obtained using a denser K-point calculation.

For switching to occur at a particular temperature via a particular path, a energy barrier has to be overcome. We have performed Nudge Elastic Band (NEB) calculations as implemented in VASP[42,43] to estimate the switching barriers. For a NEB calculation, ten intermediate images are created by interpolating between the initial and final states which are chosen as the local minima configurations obtained during relaxation.

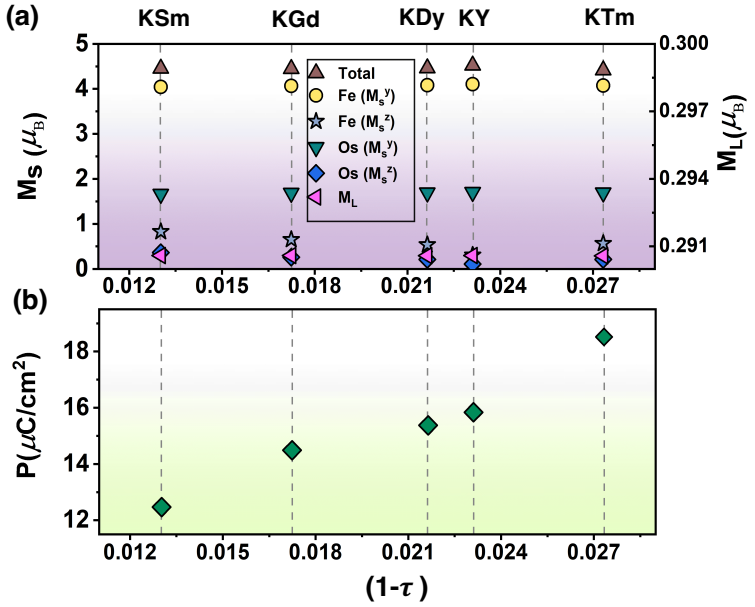

Figure 3: Variations of (a) spin and orbital magnetic moments, (b) spontaneous polarization for all the DPOs as considered in this study.

Results and discussion

Functional properties of DPOs from DFT simulations

We begin discussing our results with basic functional properties of the DPOs. The high symmetry $P4/nmm$ and low symmetry $P2_1$ phases are shown In Figure 1(a) and Figure 1(b), respectively. The functional modes are obtained after decomposing the low-symmetry $P2_1$

($a^-a^-c^+$) with respect to the high symmetry $P4/nmm$ ($a^0a^0a^0$) phase. We have plotted all the phonon instabilities (functional modes) for all the DPOs in Figure S6 of the Supporting Information. An illustration of four different structural distortions giving rise to four key functional modes such as in-phase rotation (Q_{R+}), tilt (Q_T), antiferroelectric A-site displacement (Q_{AFEA}), 2-dimensional charge disproportionation ($Q_{CD_{2D}}$) is included in Figure 1(c). The space group symmetry of $P2_1$ phase is established by three symmetry-breaking structural distortion pathways from the parent paraelectric $P4/nmm$ phase, as shown in the Figure 2(a). The three symmetry-breaking pathways are listed in the following: (i) trilinear coupling between Q_T, Q_{R+} and Q_{AFEA}, (ii) coupling between Q_{R+} and $Q_{CD_{2D}}$ (iii) coupling between Q_T and $Q_{CD_{2D}}$. Individually, Q_T, Q_{R+} and Q_{AFEA} also drive different functionalities[13,44,45] in single and DPOs. For example, Q_T drives weak ferromagnetism in (Ln,Y)FeO_3-based single perovskite oxides with $G_xA_yF_z$ magnetic configuration. Linear magnetoelectricity in both single and DPOs is driven by Q_{R+}. Q_{AFEA} drives polarization in DPOs with A/A′ cation ordering. The 2-dimensional $Q_{CD_{2D}}$ is present in the *ab*-plane. It accounts for systematic elongation and contraction of bond lengths between B-O and B′O confined within a plane to maintain neutral bonding environment. Its origin is tied to the degenerate $3d$ and $5d$ electronic states of t_{2g}, e_g electrons coming from the BO_6 and t_{2g} electrons of $B'O_6$ octahedra, respectively. This mode is responsible for tuning the charge states of magnetic B and B′ cations. It, in turn, drives metal-to-insulator transition and change of spin state.

All key mode amplitudes controlling polarization increase as (1-τ_{avg}) increases except $Q_{CD_{2D}}$ mode, which remains almost constant (see Supplementary Information, Figure S3 and Figure S4). The radius mismatch between A and A′ cations which induces stable A-site cation ordering, also get more pronounced with increase in (1-τ_{avg}). Hence, these observations imply that the polarization as well as T_c will also increase with increase in (1-τ_{avg}).

We have performed single-point energy calculations considering the variation of Q_{R+} and Q_T to obtain the energy surfaces for $KYFeOsO_6$, as shown in Figure 2(b). The energy landscape derived from these computations, results in four equivalent structural minima.

The four structural domains together with polarization P and magnetization M show possible pathways along which switching can happen. Here, $\vec{P}$ switching can take place either via Q_{R+} or Q_T, whereas $\vec{M}$ can only be switched by Q_T.

For $KLnFeOsO_6$ DPOs in low symmetry $P2_1$ phase, Fe is in +3 charge state and Os is in +5 charge state, leading to $3d^5$ and $5d^3$ electronic states, respectively. Based on the energy levels, we find that the basic structure remains the same for all KLn systems in the A-sublattice. It indicates that changes in A-sublattice does not greatly affect the electronic structure of B-sublattice. Thus, all such systems in low symmetry $P2_1$ remain insulating in nature as shown in Figure S5 of Supporting Information. The magnetic properties are governed by the electronic states of Fe^{+3} and Os^{+5} ions. Our findings show that the ground state magnetic configuration, $A_xG_yG_z$, is noncolinear in nature. The G-type antiferromagnetic (AFM) ordering between Fe and Os spins with easy axis along y-axis (along crystallographic b axis) has the most contribution towards the net magnetization. Along x and z axes, the components are of A-type (along crystallographic a axis) and G-type AFM (along crystallographic c axis), respectively, with small magnitudes. In Figure S1 of supporting information, we have shown the vector representation of $A_xG_yG_z$ magnetic configuration. The net spin magnetic moment (M_s) is $2\mu_B$/f.u. which reflects a spin state of S=1. In addition to spin magnetic moment, the $5d$ transition metals have considerable orbital moment originating from strong spin-orbit coupling. For $KYFeOsO_6$, the orbital moment (M_L) is $0.291\mu_B$. The presence of finite orbital moment, in $t_{2g} - d^3$ configuration can be rationalized in terms of mixing of unoccupied e_g states mediated through other electronic states rather strong hybridization with p states of O atoms.[46] Variation of spin components and orbital moment with respect to (1-τ) are shown in Figure 3(a). It shows that the M_s and M_L do not vary much for different DPOs.

The origin of polarization in HIF is the non cancellation of the layered polarization along two successive layers. The polarization vector $\vec{P}$ remains in the xy plane (components along crystallographic a([100] and b([010]) directions). P_{xy} increases with respect to the A-

cation radius mismatch (ΔR). It thereby establishes a relation with (1-τ_{avg}) as depicted in Figure 3(b). Magnitude of P_{xy} for DPOs studied here fall in the range of 12.4−18.5 $\mu C/cm^{-2}$. The size of the polarization is comparable to that reported for proper ferroelectric $BaTiO_3$ ranging between 14−27 $\mu C/cm^{-2}$.[47,48]

However, the most important criteria for a material to be ferroelectric lies in its (polarization vector) capability to switch by 180°. The conventional switching paths for $\vec{P}$ are via

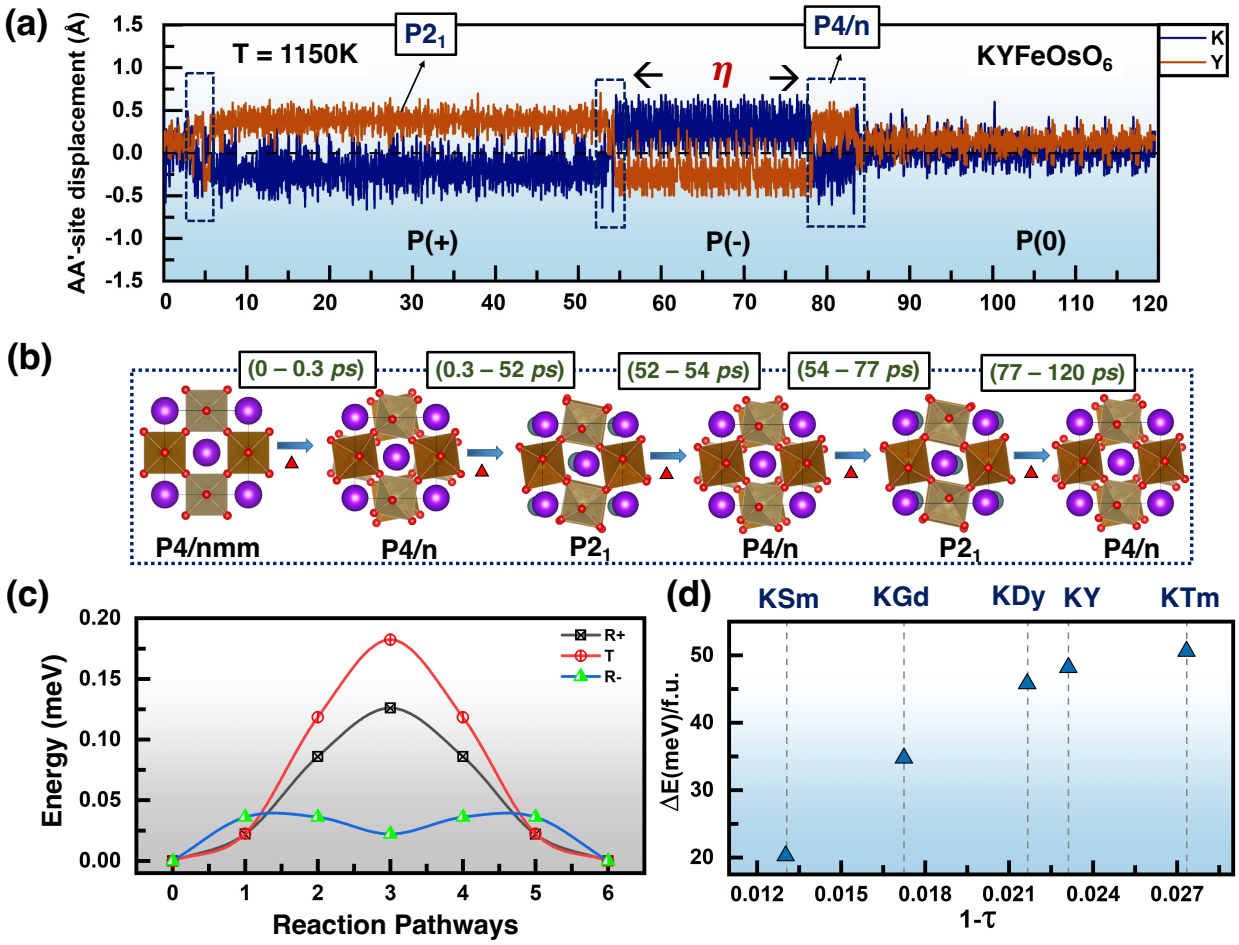

Figure 4: (a) Upper panel shows the displacement of the A, A′ sites i.e., K and Y atoms along c axis as a function of time under 1150 K for 120 ps. Snapshots of structures corresponding to $\vec{P}(+)$, during $\vec{P}(0)$, and after switching $\vec{P}$(-)of the $KYFeOsO_6$ are shown in the bottom panel. (b) Energies for reaction coordinates as computed using Nudge elastic band (NEB) for $KYFeOsO_6$. The plot shows energy barriers for three different switching paths along Q_{R+} in-phase rotation ($a^0a^0c^+$), Q_T tilt ($a^-a^-c^0$) and Q_{R-} out of phase rotation $a^0a^0c^-$ as Q_T=0, ($a^-a^-b^-$, if $Q_T \neq 0$), respectively. (c) Energy barriers for different DPOs with respect to 1-τ as obtained from NEB analyses.

tuning Q_{R+} or Q_T or an associated intermediate path as discussed in Ref.[18] Here, $Q_T(a, b)$ switches to $Q_T(a, -b)$ as shown in the energy landscape with respect to rotation and tilt distortions in Figure 2(b). Each of these paths is governed by the crystal symmetry. This picture is valid at 0 K temperature. However, in addition to possible paths, successful polarization switching requires the system to overcome an energy barrier which is often referred to as the switching barrier (ΔE). This threshold energy can be overcome by external stimuli such as electric field, temperature or optical laser excitation. If we gradually heat a HIF DPO or superlattice, it is expected to exhibit polarization switching at a finite temperature. The temperature at which the $\vec{P}$ switches is primarily triggered by the condensation of that particular structural mode responsible for switching, i.e., Q_{R+} or Q_T. But the question around other existing possible switching mechanisms at higher temperatures still remains. This sets the stage to discuss our next set of results obtained from the finite temperature AIMD simulations.

Insights from AIMD simulations

For understanding the mechanism behind $\vec{P}$ switching, we have performed finite temperature AIMD simulations at various fixed temperatures T = 100 K to 2100 K for $KYFeOsO_6$ system. During each AIMD simulation at a finite T, we have recorded the changes in displacement of A and A$'$ cations from their corresponding centrosymmetric positions. The variation in displacement magnitude with respect to centrosymmetric position $\Delta AA'$ (Å) for $KYFeOsO_6$ at T = 1150 K, as a function of the time step Δt (ps) is shown in Figure 4(a). The corresponding structural transitions are presented in Figure 4(b). During $5-52$ ps the system remains in $\vec{P}(+)$ state, whereas, from $52-54$ ps the polarization state changes to $\vec{P}$(-) and retains till 77 ps. It becomes evident that switching from $\vec{P}(+)$ to $\vec{P}$(-) is initiated at $52ps$ and completed at 54 ps. This is a signature of ultra-fast $\vec{P}$ switching as previously reported in molecular ferroelectrics.[49] For understanding the contributions of structural modes controlling the switching, we have studied the evolution of these modes

during $\vec{P}$ switching at different time snapshots throughout the simulations. We find that before (at 51 ps) and after switching (at 53 ps), the crystal structure remains in the same space group symmetry as $P2_1$. The magnitudes of the structural modes described in Figure 1 do not change before and after the switching, as expected. No additional modes appear in $\vec{P}$(+) and $\vec{P}$(-) states. The direction of Q_{R+} changes from (+) to (-) gives rise to the switching. The inherent coupling between Q_{R+}, Q_T and the polar mode (originated from AA′-sites represented by Q_{AFEA}) is still maintained in the switched phase.

Interestingly, our analysis on the duration of switching reveals that the system transforms through a centrosymmetric phase as $P4/n$ which is different from the standard high symmetry $P4/nmm$ phase. We find that $\vec{P}$(+) to $\vec{P}$(-) switching is actually a two step process. In this switching mechanism, the BO_6 and $B'O_6$ octahedra located at the top layer (here B=Fe and B′=Os) rotate first followed by a complementary rotation of these octahedra located at the bottom layer of the system. As a result, $\vec{P}$ switches from $\vec{P}$(+) to $\vec{P}$(-), as described in Figure 4(b). The intermediate state is the non-polar $P4/n$ phase in which the first rotation has already taken place. This in-between phase has Q_{R-} distortion, as represented by $a^0a^0c^-$. Thus, switching from $\vec{P}$(+) to $\vec{P}$(-) is primarily driven by Q_{R-}. There is no sign of direct switching via Q_{R+} or Q_T that takes place at finite temperatures as obtained from the AIMD simulations. This finding contradicts the conventional picture of switching mechanisms which was based on the two primary order parameters, being the controlling factors.

Further, to validate our claims from the AIMD simulations, we have calculated the switching barriers (ΔE) via Q_T, Q_{R+} and Q_{R-} pathways by Nudge elastic band (NEB) method. We have assumed Q_T=0 for computing energy barrier via Q_{R-} switching path. As shown in Figure 4(c), ΔE via Q_{R-} switching path is nearly 4 times and 3 times less than that via Q_T and Q_{R+}, respectively. It implies that for $KYFeOsO_6$ at T=1150 K, the polarization switching can only can be realized via Q_{R-} switching path. The switching via Q_{R-} shows two maxima and one intermediate minima along the reaction path. It further institutes that

the switching we observe for the DPOs is indeed a two step process where the intermediate minima is found at the optimized structure with Q_{R-} distortion.

This outcome is quite surprising, since at the time of mode decomposition of $P2_1$ phase with respect to $P4/nmm$, the Q_{R-} mode ($a^0a^0c^-$ as Q_T=0) is absent. It is further illustrated in Figure S4 of the Supporting Information. However, phonon computation performed on high symmetry $P4/nmm$ denotes Q_{R-} mode to be unstable along with the other modes (see Figure S6 and Table S6 in Supporting Information). Thus, Q_{R-} acts as a catalytic mode that facilitates the polarization switching. Further, we have investigated how $\Delta E_{Q_{R-}}$ changes as A and A′ cation radius mismatch is varied for K and Ln for DPOs, with Ln= Sm, Gd, Dy, Tm and Y. Additional details on the switching barrier ΔE, via Q_{R-} switching path, computed rotation and tilt angles are included in Figure S7 and Table S7 of the Supporting Information. We find that ΔE for Q_{R-} switching barrier increases with (1- τ) and is the highest for KTm, shown in Figure 4(d). It represents how much the system has distorted with respect to the cubic symmetry. This observation is also consistent with analysis of the structural modes, where for systems with (1- τ) $\sim$0, the in-plane rotation angle θ_{Rot} is less than that in systems with (1-τ) $>$ 0. For example, if we compare between KSm and KGd, θ_{Rot} for KSm is smaller. Hence, for KSm, it will require less energy to switch θ_{Rot} (+) to θ_{Rot} (-) than KGd.

The optimized high symmetry $P4/nmm$ phase (obtained at 0 K) of $KYFeOsO_6$ is heated up to T = 300 K for 120 *ps* in the initial set of AIMD simulations. It immediately goes to the polar $P2_1$ phase and remains as the equilibrated phase for the entirety of the simulation period. There is no reversal of polarization direction that takes place during this simulation. Polarization switching for the first time is only observed when the system is heated up to T = 1150 K. We have performed additional simulations by systematically increasing the temperature with 100 K step size from T = 100 K to establish that even at T = 1100 K, the direction of the polarization remain the same (see Figure S8 in Supporting Information). At 1200 K, all DPOs undergo polarization switching via Q_{R-}. The magnitude of polarization

components along x, y and z directions (a, b and c crystallographic axes, respectively) remain nearly the same for $\vec{P}(+)$ and $\vec{P}$(-) states (see Figure S9 and Table S8 in Supporting Information), as expected in polarization switching.

The time taken for $\vec{P}$ to switch for the first time decreases with increase in temperature, as shown in Figure 5(a). Here, we have taken $P2_1$ structure as the initial structure for the AIMD simulation. Similar behavior with a shift in the time scale is expected if the simulations is started with $P4/nmm$ structure. Once the system is heated up to a finite temperature $\geq$ 1150 K from 0 K, the energy barrier for switching to occur has already been overcome for higher temperatures. The energy barrier almost falls to zero at temperatures $\geq$ 1500 K. Beyond 1500 K, the system is equilibrated to non polar $P4/n$ phase immediately and therefore no polarization switching is observed. $\vec{P}$ is allowed to switch based on the magnitude of the energy barrier which reduces with increase in temperature, making the switching to occur faster between 1150 K to 1500 K. At T $>$ 1500 K, the in-phase rotation angle (attribute to represent Q_{R-}) becomes almost zero, driving the system into its high symmetry phase (see Figure S10 and Table S9 in Supporting Information). Consequently, the energy barrier also decreases with decrease in rotation angle. Therefore reducing the rotation angle facilitate faster switching, provided some amount of the structural distortion is still left in the system to drive it (see Figure S10 in Supporting Information).

It is crucial to increase the time of retention of the switched state (say η) to prevent the system to transform back to the non-polar phase. The way to increase η is to lower the temperature. Below the ferroelectric ordering temperature T_c, the switching will not be observed. From Figure 5(a), it is evident that the time at which the first switching takes place increases exponentially with respect to the decrease in temperature. This time approaches to infinity at T_c. The exact ordering temperature of these DPOs is not currently known. Finding T_c for all the DPOs also goes beyond the scope of this paper. However, we have derived understandings on the variation of T_c with polarization, based on a systematic literature review on the existing experimental reports while evaluating implications of such

information on our results. These reference studies [50–59] report sizeable ferroelectric order (See Table S10 in Supporting Information) at room temperature for a number of DPOs. The ferroelectric T_c is high for systems with large spontaneous polarization P, ranging between 0.36 – 24 $\mu C/cm^2$ with T_c ranging between 300 – 630 K. Previous work [59] based on Monte Carlo simulations also reveals a quadratic relation between the magnitude of spontaneous polarization and T_c; $T_c = \alpha\ |P_s^2|$. Since the magnitude of the spontaneous polarization for the DPOs in our study falls in the range between 12 – 19 $\mu C/cm^2$ corresponding T_c can be expected to be at or above room temperature. At 600 K, the non-polar $P4/n$ phase starts to appear during initial stages of the AIMD simulation. With increase in temperature, the non-polar phase persists for a longer time before the system goes to the polar $P2_1$ phase. Above 1500 K the system immediately goes to the non-polar $P4/n$ phase within a few ps of the AIMD simulation. Below 600 K the system goes to the polar phase at the very beginning of the AIMD simulation as summarized in Figure S8 of Supporting Information. Based on our analysis, we expect the T_c for $KYFeOsO_6$ may fall between 500 - 600 K. However, we cannot confirm it since it requires performing Monte Carlo simulations which goes beyond the scope of our present study.

We have analyzed the time taken for $\vec{P}$ to switch for the first time and switching cycle (number of switching within 50 ps, starting from polar $P2_1$ phase) to understand how both of these quantities vary with respect to (1- τ) signifying different DPOs at 1200 K. The results are shown in Figure 5(b) and (c), respectively. The time taken for $\vec{P}$ to switch for the first time during the entirety of the simulation increases as the difference between cation sizes at A and A$'$ sites is increased. The number of possible switching cycle reduces as the size of A$'$ decreases. It also follows our physical intuition that it is easier for smaller cations to exhibit in-phase or out-of-phase rotation which are the primary driving factors behind $\vec{P}$ switching. Hence systems with smaller cation radii size difference between A and A$'$ sites experience less hindrance to accomplish the two-step switching, allowing for more number of switching cycles to come about during the same time period of simulations. Based on our

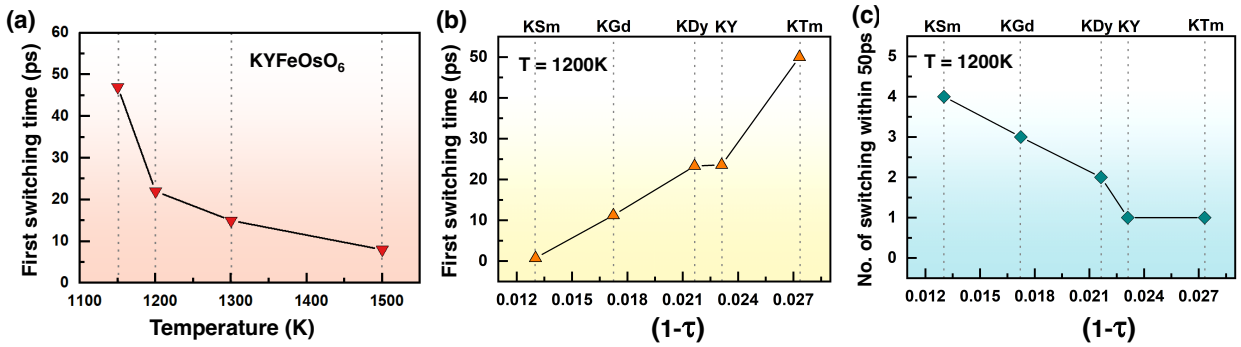

Figure 5: (a) Changes in the time taken for $\vec{P}$ to switch for the first time for $KYFeOsO_6$ with respect to temperature. Same has been plotted for all five DPOs at 1200 K as shown in (b). In addition, switching cycles as occurred within 50 *ps* with respect to temperature, for all five DPOs at 1200 K are shown (c).

analysis presented in Figure 5(b) and (c), we predict that the T_c shall follow the trend as T_c (KTm) > T_c (KY) > T_c (KDy) > T_c (KGd) > T_c (KSm) within the DPOs studied here.

Concept for potential device applications

So far we have already established that temperature dependent polarization switching is feasible in HIF DPOs. Below we have outlined how tunable functionalities of DPOs such as (a) temperature tuned $\vec{P}$ switching and (b) switching of spin state S mapped with $\vec{P}$ switching can be utilized in device applications.

Temperature dependent polarization switching

Our first proposition is a device that changes its $\vec{P}$ state from ON ($\vec{P}$(+)) to OFF ($\vec{P}$(-)) with change in temperature. It is different compared to perovskite oxides based device concepts which use the reversal of electric field as the external attribute to undergo switching. We come up with this concept based on the following set of simulations in addition to what we have learned in the previous sections. As shown in Figure 6(a), $KYFeOsO_6$ is first heated from 900 K to 1200 K followed by cooling down to 900 K. To capture the dynamics of the system during this transition, we have first performed the AIMD simulation for 50 *ps* keeping a constant temperature at 900 K. There is neither a $\vec{P}$(+) polarization state nor

$\vec{P}$ switching that occurs during this simulation or once it is completed. Next, we use the structure generated at the end of 50 *ps* at 900 K and rerun the AIMD simulation for another 31 *ps*. At this stage, the temperature is raised to 1200 K and held constant throughout the simulation. As expected, we observe $\vec{P}$ has switched its state between 66-74 *ps*. At 75 *ps*, $\vec{P}$ goes to (-) state. The simulation is continued while keeping temperature fixed at 1200K for another 7 *ps*, amounting to a total time of 81 *ps* . As the final step, we use the structure taken from the completed previous simulation, lower the temperature to 900 K and perform AIMD simulation for 130 *ps*. We notice that as the temperature is lowered to 900 K, $\vec{P}$ retains it state as $\vec{P}$(-). The $\vec{P}$ is expected to switch from (-) to (+) if the system is again heated to 1200 K. Therefore, continuing the heating/cooling cycle, (from 900 K to 1200 K) $\rightarrow$ (from 1200K to 900K) $\rightarrow$ (900K to 1200K) results in sequential $\vec{P}$(+) $\rightarrow\vec{P}$(-)$\rightarrow\vec{P}$(+) switching. This behavior is expected to continue for a long period of time until the material degrades. Till date, one logic behind designing switching devices has relied on $\vec{P}$ switching by tuning electric field. From our extended simulations, we are now able to establish an alternative way to accomplish switching by tuning temperature instead of the electric field, with potential applications in thermally active sensors and actuators.

Temperature dependent simultaneous switching of polarization and spin state

Our next postulate details how a multi-state memory device can be materialized by employing the concurrent nature of polarization and spin state switching throughout the heating/cooling cycle. Below we discuss the outputs from the simulations helpful to set the premise for conceptualizing this potential application. For $KYFeOsO_6$ in low symmetry $P2_1$ phase with G-type AFM ordering, the total magnetic moment is 2 μ_B/f.u. with S=1. The magnetization is primarily determined by Fe and Os elements which are in +3 and +5 oxidation states leading to $3d^5$ and $5d^3$ elemental configurations, respectively. As shown in Figure 6(b), we have computed S and $\vec{P}$ during the interval of the switching process (66-75 *ps*) at 1200 K. The results are quite remarkable. During the time of switching, S can have two states,

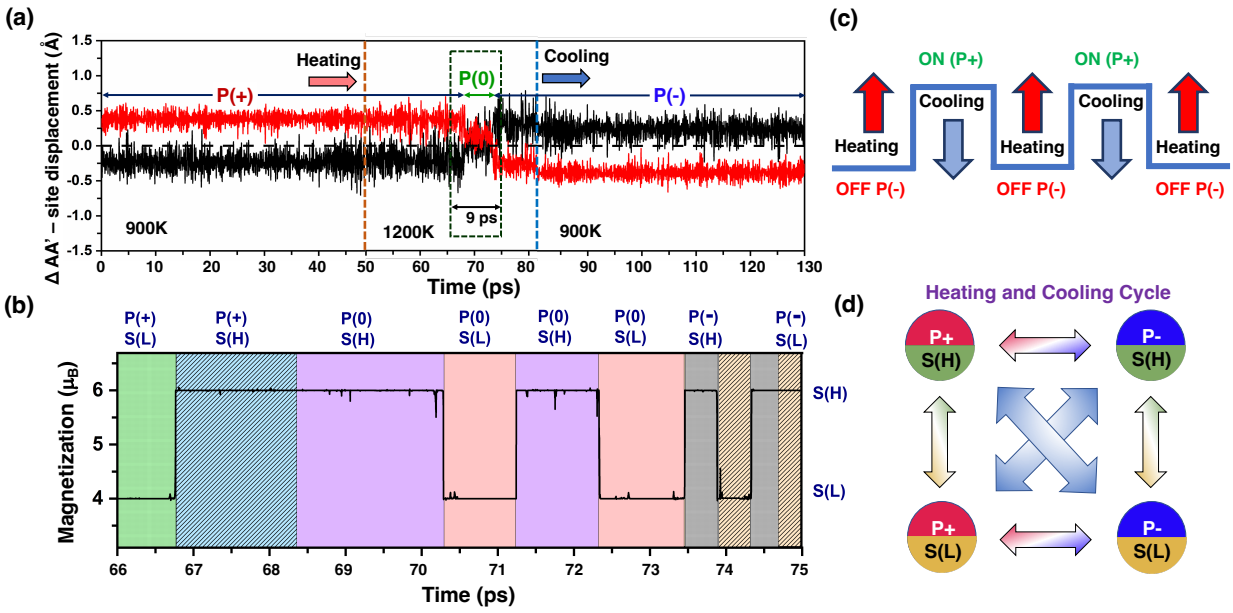

Figure 6: (a) Variation in the magnitude of displacement with respect to centrosymmetric position $\Delta AA'$ (Å) as a function of run time of AIMD simulation. (b) Changes in magnetization $\vec{M}$ and spin state $\vec{S}$ during $\vec{P}$ switching. (c) Schematic representations of proposed ON/OFF polarization switching as realized by sequential heating/cooling effect and (d) control of both polarization and spin-state within the heating/cooling cycle.

S=1 (M=2μ_B/f.u. low spin state S(L)) and S=3/2 (M=3μ_B/f.u., high spin state S(H))), whereas, $\vec{P}$ has three states $\vec{P}$(+), $\vec{P}$(0) and $\vec{P}$(-) (as switching happens during this time interval). Once combined, the system is capable to exhibit six different states such as [$\vec{P}$(+), S(L)], [$\vec{P}$(+), S(H)], [$\vec{P}$(0), S(H)], [$\vec{P}$(0), S(L)], [$\vec{P}$(0), S(H)], [$\vec{P}$(0), S(L)], [$\vec{P}$(-), S(H)], [$\vec{P}$(-), S(L)], as shown in Figure 6(b). This is where it becomes interesting where possibilities of transition between various of these states, for e.g., [$\vec{P}$(+), S(H)] $\rightarrow$ [$\vec{P}$(-), S(L)] or [$\vec{P}$(+), S(L)] $\rightarrow$ [$\vec{P}$(-), S(H)] can take place. In other words, spin state switching becomes possible via reversal of $\vec{P}$. For further demonstration, let us assume, S(H)=1, S(L)=0 and similarly $\vec{P}$(+)=1 and $\vec{P}$(-)=0. Utilizing the synchronized switching behavior of $\vec{P}$ and S, a total of four states (0,0), (1,0), (0,1) and (1,1) are now accessible, implying the concept behind a multi-state memory device. Previously, strain driven tuning of the spin state is reported in molecular magnets by first-principles calculations .[60] However, manipulation of spin state by switching of spontaneous polarization has only been proposed at the phenomenological

level.[61] We are now able to realize it at finite temperatures within the scope of our study utilizing DFT and AIMD simulations.

To understand the microscopic origin of spin state switching, we have performed total density of states (TODS) and partial density of states (PDOS) analysis of all six different spin states as shown in Figure S11 of Supporting Information. The average local magnetic moments of Fe and Os in $KYFeOsO_6$ at low spin (M_T = 2.0 μ_B/f.u, S= 1) state are 4.08 and 1.74 μ_B, respectively. The ideal magnetic moment on Fe (+3) and Os (+5) are expected to be 5.00 μ_B and 3.0 μ_B, respectively. The reduction in these moments in $KYFeOsO_6$ is due to hybridization between Fe-3d and O-2p, Os-5d and O-2p electronic states, respectively. In high spin state S=3/2, M_T is 3.0 μ_B. This is because the local magnetic moment on Os is reduced further to 1.01 μ_B which in turn increases M_T of the system in G-type spin alignment. The change in magnetization occurs due to an increase in hybridization between Os-5d and O-2p electronic states at Fermi level as shown in Figure S11 of Supporting Information. The up-spin Fe-3d levels are located deep in the valance band below -8 eV, whereas, Os-5d levels in the down spin channel is near the Fermi level. That is why hybridization between Os-5d and O$-2p$ are more sensitive to structural distortions. The increase in hybridization is also captured by the reduction of OsO_6 octahedral volume. Therefore, Os atoms contribute the most towards the changing the spin states of the system at higher temperatures. The variation in the local Os magnetic moments drives the global spin state from S= 1 to S=3/2. The local magnetic moments of Fe mostly remain the same and thus does not contribute much towards the change in spin state.

Here, we would like to point out that achieving temperature-driven polarization switching devices will be challenging in real experiments. However, we believe it is not completely impossible. The main challenge lies in reducing the temperature rapidly below switching temperature T_s, such that the time of retention of the switched polar state, can be increased. We have performed AIMD simulation at 600 K with initial state as the ground-state polar $P2_1$ phase, as shown in Figure 7. The time of the simulation is considered much longer, up

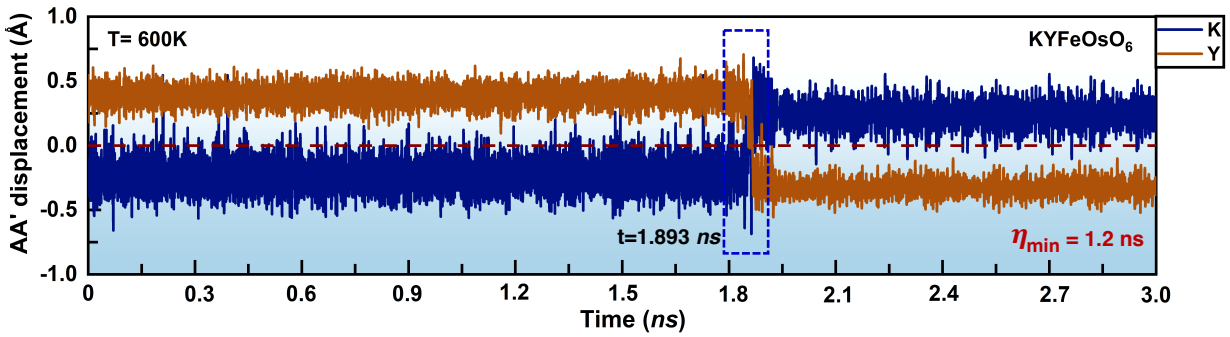

Figure 7: Variation in the magnitude of displacement with respect to centrosymmetric position $\Delta AA'$ (Å) as a function of run time of AIMD simulation at 600 K for 3 ns. The retention time η has increased to 1.2 ns at 600 K from 23 ps at 1150 K.

to 3.0ns. It is evident that the polarization direction switches after 1.893 ns and remains in that state till the end of simulation time (3.0 ns). The polarization retention time is at least 1.2ns. This is exactly what we have pointed out before about tuning the time of retention of the switching state. At higher temperature such as 1150 K, the retention time of the switched state is much less (23 ps). The temperature dependent switching is associated with the phase transition. The sequence of phase transition observed with increase of temperature as, $P2_1$ $(a^-a^-c^+) \rightarrow P4/n$ $(a^-a^-b^-) \rightarrow P4/nmm$ $(a^0a^0a^0)$. The primary order parameters of the HIF are in-phase-rotation, Q_{R+} $(a^0a^0c^+)$ and tilt Q_T $(a^0a^0c^+)$. Both modes are present in the polar ground-state $P2_1$ $(a^-a^-c^+)$ phase. However, polarization switching occurs via out of-phase-rotation, Q_{R-} $(a^-a^-b^+)$, which is not present at the lower temperature. Presence of Q_{R-} mode is essential to drive switching. Q_{R-} mode only starts to condense with the increase in temperature. At higher temperature, Q_{R-} mode will condense faster leading to $P4/n$ phase faster. Thus, at the phase boundary of $P2_1$ $(a^-a^-c^+)$ and $P4/n$, the Q_{R-} mode can be engineered to gain long retention time η (and ideally infinity). Larger retention time will provide additional time to cool down the material to a lower temperature where $P2_1$ phase is stable but with polarization switched.

From experimental point, one possible route for ultra fast cooling, is by implementing femtosecond pulsed laser, to capture these timeframes for obtaining a spin-crossover or dif-

ferent spin-states.[62] Recently, Ridier et al. showed that a photo-induced switching between the molecular low spin and high spin states, probed through the relative change of the optical transmission, typically occurs on the sub-picosecond timescale.[62] This is similar to what we observe in our results (Figure 6). There are additional examples in the literature on the ferroelectric properties of double perovskites upon heating and cooling.[63,64] A similar report on a halide double perovskite subjected to very fast heating, cooling sequence can lead to exhibition of a ferroelectric ordering.[64] Ultrafast cooling has also been demonstrated at microsecond scale for biomolecular dynamics.[65] Ultra-fast magnetic switching has already been observed and used commonly in magnetic tunnel junctions (MJT) where switching time ranges between 50ps to 500ps.[66,67] Using an optical pulse,[68] the direction of the magnetization in magnetic devices can be controlled in picoseconds range using the spin-transfer torque effect (STT).[69] Recent experimental papers have reported occurrence of ultrafast magnetization switching in metal/ferromagnetic bilayers,[70] magnetic quantum dots,[71] thin film heterostructures[72] etc., Many novel non-volatile memory applications demand such ultrafast magnetic switching for spin-transfer torque magneto resistive random-access memory (or STT-MRAM), neuromorphic computing[73] and energy harvesting.[74] Hence our proposed device concepts will have huge impact in the fields of non-volatile memory applications which needs systems with ultra-fast magnetic switching. Considering these examples, we are optimistic about the feasibility of attaining switching in a picosecond's timescale regime, as proposed in our study.

Finally, we note that the polarization switching is expected to be driven by ($a^-a^-c^+$) distortion, even for other polar phases. As for example (shown in Figure S12 of the supporting information), we have considered the A-site rock-salt and B-site rock-salt cation ordering (P_c phase) of $KYFeOsO_6$ and performed the same AIMD simulations at 1150 K for 120 *ps*. The initial structure in considered to be the non-polar $F4\bar{3}m$ phase. The system goes to the ground state non-centrosymmetric P_c phase immediately. We observe a similar polarization switching as we did in the A-site layered system. The system switches from $\vec{P}(+)$ to $\vec{P}(-)$ at

around 40 *ps* and the switched state is maintained for another 60 *ps* (still the end time of AIMD simulation). The critical point, here is that the system changes from $\vec{P}(+)$ to $\vec{P}(-)$ ($\vec{P}(-)$ to $\vec{P}(+)$) also via out-of-phase rotation. In this nonpolar phase is C_2 phase ($a^0a^0c^-$). Therefore, it is safe to say that the same switching mechanism is applicable to other phases in the same materials family irrespective of their cation ordering, if ($a^-a^-c^+$) distortion establishes a polar phase.

Conclusion

The $KLnFeOsO_6$ DPOs (Ln= Sm, Gd, Dy, Tm and Y), with A-site layered and B-site rock-salt ordering are hybrid improper ferroelectric in nature with large magnetization and polarization. Polarization switching from $\vec{P}(+)$ to $\vec{P}(-)$ in these oxides is primarily driven by Q_{R-}. It is a two step process that takes place via distortion from Q_{R+} to Q_{R-}. During switching, the BO_6 and $B'O_6$ octahedra located at the top layer rotate first from (+) to (-) followed by the rotations of the same located at the bottom layer from (-) to (+), via (0). It transforms the system to a distorted Q_{R-} structure along $a^0a^0c^-$. The polarization switching is ultra-fast in nature with a linear dependency on temperature with possibility of switching at higher temperature. The DPOs with smaller cation size difference between A and A′ sites with tolerance factor close to cubic structure (smaller rotation angle) enhances the feasibility of the two-step switching process.

The advantage of understanding how switching occurs in polar DPOs is two-fold. One is in formulating design rules for materials discovery with tunable polar and magnetic functionalities. Another lies in the potential of realization of the mechanism in device applications. As established in this work, temperature driven concurrent switching of $\vec{P}$ and spin states within a heating/cooling cycle between 900 K to 1200 K opens up alternate avenues for switching devices that are conventionally otherwise tuned by electric field. In addition, our analysis indicates a possible method to increase the time of retention (η) of the switched

state to prevent its transformation back to the non-polar phase. The retention time η has been found to increased from from 23 ps at 1150 K to 1.2 ns at 600 K. Thus, heating the sample form 500K to 600K will switch the polar state from $\vec{P}(+)$ to $\vec{P}$(-) and the system has to be cool down to 500 K again within 1.2 ns to retain the $\vec{P}$(-) state for infinite time. We propose that if we heat the sample from T_c to $T_c + \Delta T$, then η can be maximized by minimizing ΔT. Ideally, η approaches to infinity, implying complete retention of the switched state, when ΔT is infinitesimally small. Thus, it is possible to identify a critical temperature for this process to take place for a longer period of time. Overall, the insights gained from our first-principles computations conducted on a series of HIF DPOs are expected to provide a comprehensive understanding of the switching process with applications in temperature driven magnetic devices.

Author Contribution G.P. performed the DFT computations under the guidance of S.G. and A.G. M.J.S and M.S helped in discussion and additional support in calculations. A.G. and S.G. conceived the idea of the project and wrote the manuscript.

Notes The authors declare no competing financial interest.

Acknowledgements S.G and S.N acknowledges support from DST National Supercomputing Mission (NSM), Government of India, File No. DST/NSM/R&D/HPC Applications/Sanction/2021/34. S.G and G.P acknowledge DST-SERB Core Research Grant File No. CRG/2018/001728 for funding. Authors acknowledge Param Pravega supercomputer at Indian Institute of Science, Bangalore, India for providing computational support under NSM project. This research was partially supported by the Center for Nanophase Materials Sciences (CNMS), which is a U.S. Department of Energy, Office of Science User Facility at Oak Ridge National Laboratory. A.G. acknowledges NERSC for providing the supercomputing facility. This research (A.G.) was sponsored by the Laboratory Directed Research and Development Program of Oak Ridge National Laboratory, managed by UT-Battelle, LLC, for the U.S. Department of Energy. ORNL is managed by UT-Battelle, LLC, for DOE under Contract No. DE-AC05-00OR22725.

Supporting Information Available

Supporting information contains supporting figures. The following files are available free of charge.

- Table enlisting structural parameters of all $KLnFeOsO_6$ double perovskite oxides (DPOs) in $A_xG_yG_z$ magnetic configuration, where Ln = Sm, Gd, Dy, Tm (Lanthanoids) and Y (Rare earth) studied in this work (Table S1); summary of noncollinear magnetic spin moments of all $KLnFeOsO_6$ DPOs in $A_xG_yG_z$ magnetic configuration (Table S2); vector representation of Fe (black arrow) and Os (blue arrow) for $KYFeOsO_6$ spin states in noncollinear magnetic configuration, respectively (Figure S1); tabulation of spin magnetic moment and orbital magnetic moment of all $KLnFeOsO_6$ DPOs (Table S3); table listing the relative energy difference between various noncolinear magnetic configurations for $KLnFeOsO_6$ DPOs (Table S4); polarization switching observed by AIMD simulations performed for $KYFeOsO_6$, A-site layered and B-site rock salt ordering with 2×2×2 K-mesh (8 irreducible K-points)(Figure S2); comparison table of main observations from *Gamma* point calculation with that obtained from 2×2×2 K-mesh calculation. The respective AIMD simulations were performed at 1150 K for $KYFeOsO_6$ compound (Table S5); schematic representation of structural modes with irreducible representations (irrep), with snapshots of antiferroelectric O-site distortion mode (Q_{AFEO}), tilt (Q_{tilt}), in-phase rotation (Q_{R+}), 2D-charge disproportionation (CD_{2D}) and antiferroelectric A-site distortion mode (Q_{AFEA}), respectively (Figure S3); variation of mode amplitudes of $KLnFeOsO_6$ DPOs with respect to tolerance factor (Figure S3); projected density of states (PDOS) for all $KLnFeOsO_6$ where Ln = [Sm, Gd, Dy, Tm & Y] DPOs and schematic illustration of Fe+3 and Os+5 e_g and t_{2g} energy level diagram (Figure S5(a)-(e) and (f)); schematic representation of phonon instabilities for octahedral tilt + antiferroelectric A-site displacement, antiferroelectric A-site displacement along *c*-direction, in-phase octahedral rotation, in-plane antifer-

roelectric A-site displacement, out of phase octahedral rotation and octahedral tilt mode, respectively (Figure S6 (a) to (f)); details of structural distortions and imaginary phonon frequencies of $KYFeOsO_6$ (Table S6); representative figure of octahedral rotation and tilt angle of $KLnFeOsO_6$ DPOs (Figure S7); table listing rotation and tilt angles with Q_{R-} switching barriers of all $KLnFeOsO_6$ DPOs (Table S7); trajectory plot represents the displacement of the A, A′ sites i.e., K and Y atoms along c axis as a function of time from 100K - 1100 K for 120 *ps*. All of these molecular dynamics simulations start with $P4/nmm$ centrosymmetric phase (Figure S8 (a-k)); displacement of the A, A′ sites of all $KLnFeOsO_6$ double perovskite oxides from AIMD simulation performed at 1200 K. Here, we have started the AIMD simulations from the converged polar $P2_1$ structure computed at 0K (Figure S9); tabulation of polarization component before and after switching (as indicated in Figure S9), during switching polarization is always zero (Table S8); tabulation of Temperature variation of octahedral rotation angle in $P4/n$ phase(Q_{R-}, $a^-a^-b^+$ as $Q_T \neq 0$) of $KYFeOsO_6$ from AIMD simulation 100 K – 2100 K. The 0 K angle computed from density functional theory (Table S9); AIMD simulations of $KYFeOsO_6$ for T= 1200 K, 1500 K, 1800 K and 2100 K. Here, the initial structures utilized for AIMD simulations are the converged polar $P2_1$ structure computed at 0 K (Figure S10); polarization vs. T_c has been tabulated for various double and single perovskites oxides (Table S10); total and partial density of states (TDOS and PDOS) of $KYFeOsO_6$ for six spin states as [P (+), S(L)], [P (0), S(L)], [P (-), S(L)], [P (+), S(H)], [P (0), S(H)], and [P(-), S(H)] respectively, in accordance with Figure 6(b) of the main text (Figure S11); total and local magnetic moment of Fe and Os six spin states for various polarization and magnetization domains (Table S11); polarization switching observed by MD simulations performed for $KYFeOsO_6$, with A-site rock salt and B-site rock salt ordering at 1150 K (Figure S12).

References

(1) Lawes, G. Twisting and turning towards new multiferroics. *Physics* **2011**, *4*, 18.

(2) Spaldin, N. A.; Cheong, S.-W.; Ramesh, R. Multiferroics: Past, present, and future. *Phys. Today* **2010**, *63*, 38–43.

(3) Känzig, W. Ferroelectrics and antiferroeletrics. **1957**, *4*, 1–197.

(4) Shen, X.; Luo, Q.; Wu, Z.; Zhou, Y.; Wang, J.; Zhang, J.; Su, J.; Lu, X. Magnetoelectric coupling dependent on ferroelectric switching paths in two-dimensional perovskite multiferroics. *Phys. Rev. B* **2021**, *103*, L220406.

(5) Bibes, M.; Barthélémy, A. Towards a magnetoelectric memory. *Nat. Mater.* **2008**, *7*, 425–426.

(6) Burdett, J. K. Use of the Jahn-Teller theorem in inorganic chemistry. *Inorg. Chem.* **1981**, *20*, 1959–1962.

(7) Chen, Z.-X.; Chen, Y.; Jiang, Y.-S. DFT Study on Ferroelectricity of BaTiO3. *J. Phys. Chem. B* **2001**, *105*, 5766–5771.

(8) Jeong, Y. K.; Lee, J.-H.; Ahn, S.-J.; Jang, H. M. Epitaxially Constrained Hexagonal Ferroelectricity and Canted Triangular Spin Order in LuFeO3 Thin Films. *Chem. Mater.* **2012**, *24*, 2426–2428.

(9) Benedek, N. A.; Fennie, C. J. Hybrid Improper Ferroelectricity: A Mechanism for Controllable Polarization-Magnetization Coupling. *Phys. Rev. Lett.* **2011**, *106*, 107204.

(10) Rondinelli, J. M.; Fennie, C. J. Ferroelectricity: Octahedral Rotation-Induced Ferroelectricity in Cation Ordered Perovskites (Adv. Mater. 15/2012). *Adv. Mater.* **2012**, *24*, 1918–1918.

(11) Mulder, A. T.; Benedek, N. A.; Rondinelli, J. M.; Fennie, C. J. Turning ABO3 antiferroelectrics into ferroelectrics: design rules for practical rotation-driven ferroelectricity in double perovskites and A3B2O7 Ruddlesden-Popper compounds. *Adv. Funct. Mater.* **2013**, *23*, 4810–4820.

(12) Liu, X.; Lu, J.; Chen, B.; Zhang, B.; Chen, X. Hybrid improper ferroelectricity and possible ferroelectric switching paths in Sr3Hf2O7. *J. Appl. Phys.* **2019**, *125*, 114105.

(13) Shaikh, M.; Karmakar, M.; Ghosh, S. Strain-tuned properties of hybrid improper ferroelectric superlattices through first-principles calculations and machine learning. *Phys. Rev. B* **2020**, *101*, 054101.

(14) Saha-Dasgupta, T. Double perovskites with 3d and 4d/5d transition metals: compounds with promises. *Mater. Res. Express* **2020**, *7*, 014003.

(15) Shimakawa, Y.; Azuma, M.; Ichikawa, N. Multiferroic compounds with double-perovskite structures. *Materials* **2011**, *4*, 153–168.

(16) Young, J.; Stroppa, A.; Picozzi, S.; Rondinelli, J. M. Tuning the ferroelectric polarization in AA MnWO 6 double perovskites through A cation substitution. *Dalton Trans.* **2015**, *44*, 10644–10653.

(17) Ghosh, A.; Palanichamy, G.; Trujillo, D. P.; Shaikh, M.; Ghosh, S. Insights into Cation Ordering of Double Perovskite Oxides from Machine Learning and Causal Relations. *Chem. Mater.* **2022**, *34*, 7563–7578.

(18) Zanolli, Z.; Wojdeł, J. C.; Íñiguez, J.; Ghosez, P. Electric control of the magnetization in $BiFeO_3/LaFeO_3$ superlattices. *Phys. Rev. B* **2013**, *88*, 060102.

(19) Mercy, A.; Bieder, J.; Íñiguez, J.; Ghosez, P. Structurally triggered metal-insulator transition in rare-earth nickelates. *Nat. Commun.* **2017**, *8*, 1–6.

(20) Smith, K.; Nowadnick, E.; Fan, S.; Khatib, O.; Lim, S. J.; Gao, B.; Harms, N.; Neal, S.; Kirkland, J.; Martin, M., et al. Infrared nano-spectroscopy of ferroelastic domain walls in hybrid improper ferroelectric Ca3Ti2O7. *Nat. Commun.* **2019**, *10*, 1–9.

(21) Nowadnick, E. A.; Fennie, C. J. Domains and ferroelectric switching pathways in $Ca_3Ti_2O_7$ from first principles. *Phys. Rev. B* **2016**, *94*, 104105.

(22) Huang, F.-T.; Xue, F.; Gao, B.; Wang, L.; Luo, X.; Cai, W.; Lu, X.-Z.; Rondinelli, J.; Chen, L.; Cheong, S.-W. Domain topology and domain switching kinetics in a hybrid improper ferroelectric. *Nat. Commun.* **2016**, *7*, 1–9.

(23) Li, S.; Birol, T. Suppressing the ferroelectric switching barrier in hybrid improper ferroelectrics. *npj Computational Materials* **2020**, *6*, 168.

(24) Hohenberg, P.; Kohn, W. Inhomogeneous electron gas. *Phys. Rev.* **1964**, *136*, B864.

(25) Anisimov, V. I.; Aryasetiawan, F.; Lichtenstein, A. First-principles calculations of the electronic structure and spectra of strongly correlated systems: the LDA+ U method. *Journal of Physics: Condensed Matter* **1997**, *9*, 767.

(26) Kresse, G.; Furthmüller, J. Efficient iterative schemes for ab initio total-energy calculations using a plane-wave basis set. *Phys. Rev. B* **1996**, *54*, 11169.

(27) Kroumova, E.; Aroyo, M.; Perez-Mato, J.; Ivantchev, S.; Igartua, J.; Wondratschek, H. PSEUDO: a program for a pseudosymmetry search. *J. Appl. Crystallogr.* **2001**, *34*, 783–784.

(28) Perdew, J. P.; Ruzsinszky, A.; Csonka, G. I.; Vydrov, O. A.; Scuseria, G. E.; Constantin, L. A.; Zhou, X.; Burke, K. Restoring the Density-Gradient Expansion for Exchange in Solids and Surfaces. *Phys. Rev. Lett.* **2008**, *100*, 136406.

(29) Bransden, B. H.; Joachain, C. J. *Physics of atoms and molecules*; Pearson Education India, 2003.

(30) King-Smith, R.; Vanderbilt, D. Theory of polarization of crystalline solids. *Phys. Rev. B* **1993**, *47*, 1651.

(31) Klarbring, J.; Simak, S. I. Nature of the octahedral tilting phase transitions in perovskites: A case study of $CaMnO_3$. *Phys. Rev. B* **2018**, *97*, 024108.

(32) Sepliarsky, M.; Phillpot, S. R.; Streiffer, S. K.; Stachiotti, M. G.; Migoni, R. L. Polarization reversal in a perovskite ferroelectric by molecular-dynamics simulation. *Appl. Phys. Lett.* **2001**, *79*, 4417–4419.

(33) Shimojo, F.; Hoshino, K.; Okazaki, H. First-principles molecular-dynamics simulation of proton diffusion in perovskite oxides. *Solid State Ion* **1998**, *113-115*, 319–323.

(34) Swamynadhan, M. J.; Ghosh, S. Designing multifunctional two-dimensional layered transition metal phosphorous chalcogenides. *Phys. Rev. Materials* **2021**, *5*, 054409.

(35) Brehm, J. A.; Neumayer, S. M.; Tao, L.; O'Hara, A.; Chyasnavichus, M.; Susner, M. A.; McGuire, M. A.; Kalinin, S. V.; Jesse, S.; Ganesh, P.; Pantelides, S. T.; Maksymovych, P.; Balke, N. Tunable quadruple-well ferroelectric van der Waals crystals. *Nat. Mater.* **2020**, *19*, 43–48.

(36) Nosé, S. A molecular dynamics method for simulations in the canonical ensemble. *Mol. Phys.* **1984**, *52*, 255–268.

(37) Kresse, G.; Hafner, J. Ab initio molecular dynamics for open-shell transition metals. *Phys. Rev. B* **1993**, *48*, 13115.

(38) Kresse, G.; Furthmüller, J.; Hafner, J. Theory of the crystal structures of selenium and tellurium: the effect of generalized-gradient corrections to the local-density approximation. *Phys. Rev. B* **1994**, *50*, 13181.

(39) The Maxwell–Boltzmann distribution. *Mol. Phys.* **2005**, *103*, 2821–2828.

(40) Kirov, A. K.; Aroyo, M. I.; Perez-Mato, J. M. *NEUTRON*: a program for computing phonon extinction rules of inelastic neutron scattering and thermal diffuse scattering experiments. *J. Appl. Crystallogr.* **2003**, *36*, 1085–1089.

(41) Kroumova, E.; Aroyo, M. I.; Perez-Mato, J. M.; Ivantchev, S.; Igartua, J. M.; Wondratschek, H. *PSEUDO*: a program for a pseudosymmetry search. *J. Appl. Crystallogr.* **2001**, *34*, 783–784.

(42) Henkelman, G.; Uberuaga, B. P.; Jónsson, H. A climbing image nudged elastic band method for finding saddle points and minimum energy paths. *J. Chem. Phys.* **2000**, *113*, 9901–9904.

(43) Henkelman, G.; Jónsson, H. Improved tangent estimate in the nudged elastic band method for finding minimum energy paths and saddle points. *J. Chem. Phys.* **2000**, *113*, 9978–9985.

(44) White, R. L. Review of Recent Work on the Magnetic and Spectroscopic Properties of the Rare-Earth Orthoferrites. *J. Appl. Phys.* **1969**, *40*, 1061–1069.

(45) Weingart, C.; Spaldin, N.; Bousquet, E. Noncollinear magnetism and single-ion anisotropy in multiferroic perovskites. *Phys. Rev. B* **2012**, *86*, 094413.

(46) Jia, C.; Onoda, S.; Nagaosa, N.; Han, J. H. Microscopic theory of spin-polarization coupling in multiferroic transition metal oxides. *Phys. Rev. B* **2007**, *76*, 144424.

(47) Zhong, W.; Vanderbilt, D.; Rabe, K. M. Phase Transitions in $BaTiO_3$ from First Principles. *Phys. Rev. Lett.* **1994**, *73*, 1861–1864.

(48) Diéguez, O.; Tinte, S.; Antons, A.; Bungaro, C.; Neaton, J. B.; Rabe, K. M.; Vanderbilt, D. Ab initio study of the phase diagram of epitaxial $BaTiO_3$. *Phys. Rev. B* **2004**, *69*, 212101.

(49) Tang, Y.-Y.; Zhang, W.-Y.; Li, P.-F.; Ye, H.-Y.; You, Y.-M.; Xiong, R.-G. Ultrafast Polarization Switching in a Biaxial Molecular Ferroelectric Thin Film: [Hdabco]ClO4. *J. Am. Chem. Soc.* **2016**, *138*, 15784–15789, PMID: 27934003.

(50) Alam, M.; Mandal, K. Room temperature ferromagnetism and ferroelectricity in double perovskite Y2NiMnO6 thin film. *J. Magn. Magn. Mater.* **2020**, *512*, 167062.

(51) Ravi, S.; Senthilkumar, C. Room temperature multiferroicity in a new Ba2FeMnO6 double perovskite material. *Ceram. Int.* **2017**, *43*, 14441–14445.

(52) Das, N.; Singh, S.; Joshi, A. G.; Thirumal, M.; Reddy, V. R.; Gupta, L. C.; Ganguli, A. K. Pr2FeCrO6: A type I multiferroic. *Inorg. Chem.* **2017**, *56*, 12712–12718.

(53) Gou, G.; Charles, N.; Shi, J.; Rondinelli, J. M. A-site ordered double perovskite CaMnTi2O6 as a multifunctional piezoelectric and ferroelectric–photovoltaic material. *Inorg. Chem.* **2017**, *56*, 11854–11861.

(54) Aimi, A.; Mori, D.; Hiraki, K.-i.; Takahashi, T.; Shan, Y. J.; Shirako, Y.; Zhou, J.; Inaguma, Y. High-pressure synthesis of A-site ordered double perovskite CaMnTi2O6 and ferroelectricity driven by coupling of A-site ordering and the second-order Jahn–Teller effect. *Chem. Mater.* **2014**, *26*, 2601–2608.

(55) Wang, N.; Luo, X.; Han, L.; Zhang, Z.; Zhang, R.; Olin, H.; Yang, Y. Structure, performance, and application of BiFeO 3 nanomaterials. *Nanomicro Lett.* **2020**, *12*, 1–23.

(56) Su, J.; Yang, Z.; Lu, X.; Zhang, J.; Gu, L.; Lu, C.; Li, Q.; Liu, J.-M.; Zhu, J. Magnetism-driven ferroelectricity in double perovskite Y2NiMnO6. *ACS Appl. Mater. Interfaces.* **2015**, *7*, 13260–13265.

(57) Akishige, Y.; Oomi, G.; Yamaoto, T.; Sawaguchi, E. Dielectric properties of ferroelectric hexagonal BaTiO3. *J. Phys. Soc.* **1989**, *58*, 930–939.

(58) Sharma, G.; Saha, J.; Kaushik, S.; Siruguri, V.; Patnaik, S. Magnetism driven ferroelectricity above liquid nitrogen temperature in Y2CoMnO6. *Appl. Phys. Lett.* **2013**, *103*, 012903.

(59) Fei, R.; Kang, W.; Yang, L. Ferroelectricity and phase transitions in monolayer group-IV monochalcogenides. *Phys. Rev. Lett.* **2016**, *117*, 097601.

(60) Bhandary, S.; Ghosh, S.; Herper, H.; Wende, H.; Eriksson, O.; Sanyal, B. Graphene as a Reversible Spin Manipulator of Molecular Magnets. *Phys. Rev. Lett.* **2011**, *107*, 257202.

(61) Kim, N.; Kim, H.; Kang, T. W. Manipulation of spin states by dipole polarization switching. *Appl. Phys. Lett.* **2007**, *91*, 113504.

(62) Ridier, K.; Bas, A.-C.; Shalabaeva, V.; Nicolazzi, W.; Salmon, L.; Molnár, G.; Bousseksou, A.; Lorenc, M.; Bertoni, R.; Collet, E., et al. Finite size effects on the switching dynamics of spin-crossover thin films photoexcited by a femtosecond laser pulse. *Adv. Mater.* **2019**, *31*, 1901361.

(63) Zhang, H.-Y.; Zhang, Z.-X.; Song, X.-J.; Chen, X.-G.; Xiong, R.-G. Two-dimensional hybrid perovskite ferroelectric induced by perfluorinated substitution. *J. Am. Chem. Soc.* **2020**, *142*, 20208–20215.

(64) Liao, W.-Q.; Zhang, Y.; Hu, C.-L.; Mao, J.-G.; Ye, H.-Y.; Li, P.-F.; Huang, S. D.; Xiong, R.-G. A lead-halide perovskite molecular ferroelectric semiconductor. *Nat. Commun.* **2015**, *6*, 7338.

(65) Polinkovsky, M. E.; Gambin, Y.; Banerjee, P. R.; Erickstad, M. J.; Groisman, A.; Deniz, A. A. Ultrafast cooling reveals microsecond-scale biomolecular dynamics. *Nat. Commun.* **2014**, *5*, 5737.

(66) Tulapurkar, A.; Devolder, T.; Yagami, K.; Crozat, P.; Chappert, C.; Fukushima, A.; Suzuki, Y. Subnanosecond magnetization reversal in magnetic nanopillars by spin angular momentum transfer. *Appl. Phys. Lett.* **2004**, *85*, 5358–5360.

(67) Papusoi, C.; Delaët, B.; Rodmacq, B.; Houssameddine, D.; Michel, J.-P.; Ebels, U.; Sousa, R.; Buda-Prejbeanu, L.; Dieny, B. 100 ps precessional spin-transfer switching of a planar magnetic random access memory cell with perpendicular spin polarizer. *Appl. Phys. Lett.* **2009**, *95*, 072506.

(68) Igarashi, J.; Zhang, W.; Remy, Q.; Díaz, E.; Lin, J.-X.; Hohlfeld, J.; Hehn, M.; Mangin, S.; Gorchon, J.; Malinowski, G. Optically induced ultrafast magnetization switching in ferromagnetic spin valves. *Nat. Mater.* **2023**, 1–6.

(69) Slonczewski, J. C. Current-driven excitation of magnetic multilayers. *J. Magn. Magn. Mater.* **1996**, *159*, L1–L7.

(70) Garello, K.; Avci, C. O.; Miron, I. M.; Baumgartner, M.; Ghosh, A.; Auffret, S.; Boulle, O.; Gaudin, G.; Gambardella, P. Ultrafast magnetization switching by spin-orbit torques. *Appl. Phys. Lett.* **2014**, *105*, 212402.

(71) El-Ghazaly, A.; Tran, B.; Ceballos, A.; Lambert, C.-H.; Pattabi, A.; Salahuddin, S.; Hellman, F.; Bokor, J. Ultrafast magnetization switching in nanoscale magnetic dots. *Appl. Phys. Lett.* **2019**, *114*, 232407.

(72) Gorchon, J.; Hehn, M.; Malinowski, G.; Mangin, S. Electronic transport induced ultrafast magnetization switching. *J. Magn. Magn. Mater.* **2022**, 169919.

(73) Torrejon, J.; Riou, M.; Araujo, F. A.; Tsunegi, S.; Khalsa, G.; Querlioz, D.; Bortolotti, P.; Cros, V.; Yakushiji, K.; Fukushima, A., et al. Neuromorphic computing with nanoscale spintronic oscillators. *Nature* **2017**, *547*, 428–431.

(74) Sharma, R.; Mishra, R.; Ngo, T.; Guo, Y.-X.; Fukami, S.; Sato, H.; Ohno, H.; Yang, H. Electrically connected spin-torque oscillators array for 2.4 GHz WiFi band transmission and energy harvesting. *Nat. Commun.* **2021**, *12*, 2924.

Graphical TOC Entry